https://dx.doi.org/10.1016/j.compfluid.2021.104844

Droplet impact on nano-textured bumps: Topology effects

Shakeel Ahmad[a,b], Jiyun Zhao[b], Aamer Shahzad[c], Muhammad Nafees Mumtaz Qadri[c], Hui Tang[a*]

a Research Center for Fluid-Structure Interactions, Department of Mechanical Engineering, The Hong Kong Polytechnic University, Hong Kong, China

b Department of Mechanical Engineering, City University of Hong Kong, Hong Kong, China

c Department of Aerospace Engineering, College of Aeronautical Engineering, National University of Sciences & Technology, Pakistan

*Corresponding author. Email: h.tang@polyu.edu.hk

Abstract

Using the lattice Boltzmann method (LBM), the dynamics of a single droplet impacting on desert-beetle inspired, super-hydrophobic, nano-textured bumps was numerically investigated. The focus was placed on the effects of post height, inter-post spacing, bump radius of curvature and impact velocity represented by the Weber number. Three droplet states after the impact were captured, i.e., the suspended Cassie state, the sticky Wenzel state and rebound. The interfaces among these states were then determined in parametric maps generated from the current study. Since the droplets in the Cassie state can be easily removed from the surface and thus favorable for water collection. The conditions satisfied for this state by the geometrical parameters and the Weber number were explored. The results showed that, at moderate impact speeds, droplets impacting on nano-textured bumps with sufficiently high posts or sufficiently small inter-post spacing were generally in the Cassie state and hence favorable for water collection. If these conditions are satisfied, the bump surface curvature only plays a marginal role.

Keywords: Nano-textured bump; Droplet impact; Water collection; Lattice Boltzmann method.

1. Introduction

Water demand is ever increasing with world's growing population. Around one third of total population are facing water shortage problem [1]. In such a situation fog harvesting can be a viable, sustainable and potential source of water. In nature plants and animals have skilled the survival abilities to collect water from fog. For example, the Namib desert beetles can live in area with very little rainfall [2]. Their back is composed of bumpy hydrophilic/super-hydrophobic patterns, i.e., the hydrophilic bumps are surrounded by super-hydrophobic valleys featuring microstructures of flattened hemispheres, which assist in collection of passing by fog droplets [3].

Inspired by this kind of beetles, several surfaces have been mimicked and investigated for condensation process [4–7]. However, in fog harvesting process, droplet impact is another leading phenomenon for water collection [8]. Therefore, a surface with the best overall water collection efficiency should perform well for both condensation and droplet impact processes.

Droplet impact on smooth as well as textured surfaces has been widely investigated. Normal impacts have been comprehensively reviewed by Yarin [9]. In addition to level surfaces, several works on single and multiple droplets impact on inclined surfaces have also been conducted in the past [10–14]. Recently, several studies have been conducted to investigate droplet impact on smooth convex surfaces [15–17]. Liu et al. [16] studied droplet impact on Echevaria leaves, which have convex/concave architecture. Their results showed nearly 40% reductions in contact time owing to asymmetric bounce off. Khojasteh et al. [17] studied droplet impact on hydrophobic and super-hydrophobic hemispherical surfaces and focused on the effects of Weber number, surface curvature and contact angle. They found higher area of liquid in contact with the hemispherical surface compared to flat surfaces.

Apart from smooth surfaces, droplet impact on level textured surfaces has also been investigated [18–26]. Wang et al. [23] investigated water droplet impacts on super-hydrophobic carbon nanotube arrays with different wetting properties, and found droplet rebound at contact angle 163° and no rebound at contact angle 140°. Aria and Gharib [24] studied droplet impact dynamics on super-hydrophobic carbon nanotube arrays by focusing on the critical Weber number, coefficient of restitution, spreading factor and contact time. Their results showed excellent water repellency with no droplet pinning. Kwak et al. [25] looked at the effects of droplet velocity, surface wettability, Weber number and the surface free energy on droplet impact on nano-textured surfaces, and developed a relationship for transitions from rebound to wetting and from rebound to splashing regimes. Tsai et al. [26] experimentally investigated droplet impingement on super-hydrophobic surfaces with similar contact angles but different surface roughness, i.e., one surface with regular polymeric micro-patterns and the other with rough carbon nanofibers. Similar outcomes, including the Cassie state, complete rebound, partial rebound, trapping of an air bubble, jetting, and sticky vibrating water balls, were observed at small Weber numbers for both surfaces. However, at larger Weber numbers, the splashing impacts forming several satellite droplets were observed to be more favorable for rough carbon nanofiber surfaces.

Besides, Shen et al. [27] studied millimeter-scale droplet impingement on a convex super-hydrophobic surface consisting of hierarchical micro-nano structures, and found quicker rebound compared to flat surfaces and a reduction of 28.5% in the contact time. However, in their study effects of post dimensions such as inter-post spacing, post width and height, surface curvature and impact velocity were not investigated.

Different from the above studies, the current work is focused on fog droplet impact dynamics on micro-scale bumps with nanotextures, inspired from desert beetle super-hydrophobic surface's micro-scale hemispherical bumps. The state of droplet subsequent to the impact can be crucial to water collection. A droplet impacting on nano-textured bumps can either rebound or deposit. The rebounding droplet jumps back to atmosphere, and is hence lost, which reduces the water collection rate. On the other hand, the deposited droplet can have two possible states: the Cassie–Baxter state (droplet remains suspended on the nanostructures) or the Wenzel state (droplet penetrates the nanostructures and touches the bottom surface). Droplet in the Cassie state can be easily removed from the surface and thus more favorable for water collection, while the wetting and rebounding droplets may degrade the surface's water collection efficiency. The state of droplet after the impact depends on the bump geometrical parameters and impact velocity. Therefore, in the present study the focus is placed on the effects of Weber number, post height, inter-post spacing and bump surface curvature on the droplet impact dynamics. We aim to find the relationships between bump geometrical parameters and Weber number, so as to determine the parameter ranges where the Cassie state is promoted. These parameter ranges are helpful in the design of bumps for better water collection.

2. Problem Description

Fig. 1 shows a schematic diagram of the problem. A droplet of diameter D impacts on a bump with a velocity v, where the bump surface is made of nano-posts. The dynamics of the droplet impact is influenced by the following key parameters: the gas density ρ_g and viscosity μ_g, the liquid droplet diameter D, density ρ, viscosity μ, surface tension σ, intrinsic contact angle θ_o, impact velocity v, height h and width w of the nano-post and the bump radius R.

The fog droplets vary in size $(1\sim50\ \mu m)$ [8,28], and generally, the fog droplet-size distributions have a single peak with a mode in the 10 to 14 μm range [28], while the larger droplets contribute only little to fog liquid water content. In this study, the droplet diameter is fixed at D = 10 μm. The post dimensions are selected according to literature [29–31] as follows: height up to h = 5000 nm, inter-post spacing s = 400 ~ 2000 nm and post width fixed at w = 400 nm. The dimensionless bump curvature is varied from w/R = 1/180 to 1/15. The intrinsic contact angle is taken as θ_o = 110°. Due to the numerical stability consideration, the liquid-to-gas density and viscosity ratios are set as $\rho/\rho_g = \mu/\mu_g$ = 114.5, instead of the actual ratios in nature. In previous studies the wind speed for fog harvesting ranges from 1 to 9 m/s [28,32], which can be even higher depending on the location. In this study, the droplet impact velocity v varies from 1 to 15 m/s. Its effects are studied through varying the Weber number (We), the ratio of the droplet inertia to its surface tension

$$\mathrm{We} = \rho U^2 D/\sigma \tag{1}$$

The effect of gravity is described by the Bond number as

$$\mathrm{Bo} = \Delta\rho g D^2/\sigma \sim 0.12\times10^{-6} \tag{2}$$

where g is gravitational acceleration. Since Bo is very small in the present study, the effect of gravity is neglected. Moreover, the surface tension is fixed at 0.04.

To describe the dynamics of impacting droplets, non-dimensional spreading factors along the x axis (horizontal) and y axis (vertical), respectively, are defined as

$$S_x^* = S_x/D \tag{3}$$

$$S_y^* = S_y/D \tag{4}$$

where S_x is the x spreading length defined as the horizontal distance between the two contact lines on the surface with bump radius R, and S_y is the y spreading length defined as the vertical distance from the top of the bump to either of the two contact lines on the surface with bump radius R (see Fig.1).

Moreover, a non-dimensional time t^* is employed to describe temporal events

$$t^* = vt/D \tag{5}$$

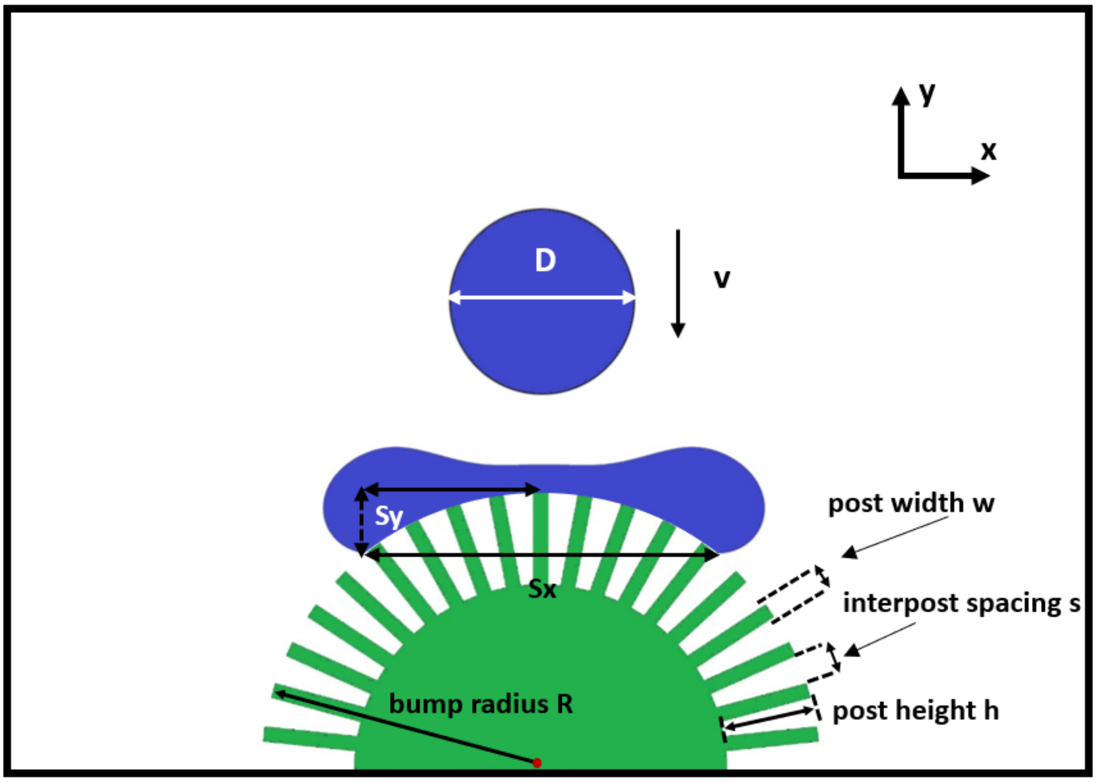

Fig. 1. Droplet impact on hemispherical nano-textured bump.

3. Methodology

In the present study, the multiple-relaxation-time lattice Boltzmann method (MRT-LBM) based on the model in Li et al. [34] is used. The fundamentals of LBM have been explained in many review articles [35,36] and monographs [37,38], and therefore are only briefly introduced here. The Shan-Chen [39] model achieves phase separation through incorporation of interparticle interaction forces. However, this model suffers from numerical instability at low viscosity. The current MRT-LBM model uses an improved forcing scheme to achieve thermodynamic consistency at relatively larger density ratios and Reynolds numbers. The wetting characteristics of the surface are achieved by computing a specific adhesion force between the gas/liquid phase and solid walls as explained in Benzi et al. [40].

The MRT-LBM is briefly explained for the brevity purpose and more information can be obtained from the reference [34]. The lattice Boltzmann equation with the MRT collision operator can be written as follows [41]:

$$f_\alpha(\boldsymbol{x}+e_\alpha\delta_t, t+\delta_t) = f_\alpha(x,t) - (M^{-1}\Lambda M)_{\alpha\beta}\left(f_\beta - f_\beta^{eq}\right) + \delta_t \acute{F}_\alpha \tag{6}$$

where $f_\alpha(x,t)$ is the density distribution function and f_β^{eq} is the equilibrium distribution function, $\boldsymbol{e_\alpha}$ is the particle velocity at position $\boldsymbol{x}$, M is an orthogonal transformation matrix [42], $\acute{F}_\alpha$ is the forcing term.

Using the transformation matrix M, the equation Eq. (6) can be written as

$$m^* = m - \Lambda(m - m^{eq}) + \delta_t\left(I - \frac{\Lambda}{2}\right)S \tag{7}$$

where $m = Mf$ and $m^{eq} = Mf^{eq}$ represent the moment space of the distribution function. I is the unit tensor the and $\left(I - \frac{\Lambda}{2}\right)S = M\acute{F}$ is the force in the moment space. The collision and streaming process is expressed as

$$f_\alpha(\boldsymbol{x}+e_\alpha, t+\delta_t) = f_a^*(x,t) \tag{8}$$

The equilibria $\mathbf{m^{eq}}$ is given as

$$\mathbf{m^{eq}} = \rho\left(1, -2+3|v|^2, 1-3|v|^2, v_x, -v_x, v_y, -v_y, v_x^2 - v_y^2, v_x v_y\right)^T \tag{9}$$

where $|v|^2 = v_x^2 + v_y^2$

The macroscopic density and velocity are calculated as

$$\rho = \sum_\alpha f_\alpha \tag{10}$$

$$\rho\mathbf{v} = \sum_\alpha e_\alpha f_\alpha + \frac{\delta_t}{2}\mathbf{F} \tag{11}$$

where $\mathbf{F} = (F_x, F_y)$ represent the total force, which includes the interparticle interaction force F_{int} and fluid-solid interaction force F_{ads}[40].

The interparticle interaction force, which causes the phase segregation is given as follows [39,43]

$$F_{int} = -G\psi(x)\sum_\alpha w(|e_\alpha|^2)\,\psi(x+e_\alpha)e_\alpha \tag{12}$$

where G is the interaction strength and $w(|e_\alpha|^2)$ are the weights. $\psi(x)$ is The effective mass [34]. An improved forcing scheme [34] is used to incorporate the forces

$$S = \begin{bmatrix} 6\mathbf{v}\cdot\mathbf{F} + \frac{\gamma|F_m|^2}{\psi^2\delta_t(\tau_e - 0.5)} \\ -6\mathbf{v}\cdot\mathbf{F} - \frac{\gamma|F_m|^2}{\psi^2\delta_t(\tau_e - 0.5)} \\ F_x \\ -F_x \\ F_y \\ -F_y \\ 2(v_y F_y - v_y F_y) \\ v_x F_y - v_y F_x \end{bmatrix} \tag{13}$$

where $\mathbf{F}$ denotes the total force, $\mathbf{v}$ is the fluid velocity, γ is tuning parameter for the mechanical stability and $|F_m|^2 = F_{m,x}^2 + F_{m,y}^2$.

3.1.Computational domain and boundary conditions

The computational domain is a two-dimensional rectangular box (1800 x 1800) (Fig. 1). Periodic boundary conditions are applied on the left and right sides of the domain. The half-way bounce-back method is employed on the top and bottom sides as well as on the post surfaces to realize the no-slip boundary condition.

A grid independence test has been conducted using four different sets of lattice-unit-to-physical-unit conversion factors. Changing the conversion factor affects the droplet spreading and retraction dynamics. Simulations are conducted for droplet impacts with initial diameter D = 10 μm on bumps with post height h = 3000 nm and width w = 400 nm, inter-post spacing s = 800 nm, and bump radius R = 45 μm. Both the maximum horizontal and maximum vertical spreading factors are listed in Table 1. It is seen that the values produced from the conversion factor of 1 lu = 20 nm has the relative errors less than 1% compared to those from the smallest conversion factor 1 lu = 12.5 nm. Hence, it is selected for the following simulations. Furthermore, to check the boundary effects on droplet dynamics a simulation case with large grid size (3600 x 3600) is conducted. The relative errors of -0.45% and -0.6% are found for the maximum spreading factors along x-axis and y-axis, respectively, for the small grid (1800 x 1800) with respect to larger grid, showing the boundary effects on maximum spreading factors are small.

Table 1 Results of grid independence tests

Lattice to physical unit conversion factor	1 lu = 40 nm	1 lu = 25 nm	1 lu = 20 nm	1 lu = 12.5 nm
Max S_x^*	1.96	1.765	1.748	1.74
Relative error (%)	-12.64	-1.43	-0.45	-
Max S_y^*	-0.1	-0.0824	-0.082	-0.0825
Relative error (%)	-21.2	0.12	0.60	-

3.2. Validation

The simulated impact and subsequent rebound of a droplet on a micro-textured surface are compared with experimental results. Bobinski et al. [44] studied a droplet of diameter D = 0.6 mm impacting and rebounding with a Weber number 2.6 on a micro-structure of post height h = 10 μm, post width w = 8 μm and inter-post spacing s = 22 μm. The impact velocity corresponding to Weber number 2.6 gives the Reynolds number Re ~ 336 for the deionized water droplet. Due to limitations of numerical method, some of the parameters are adjusted, such as the density and viscosity ratios different from those between water and air are used (see section 2), to obtain the We = 2.6 and Re ~ 336 in the simulations. The LBM simulations are conducted and the snapshots of droplet evolution at selected instants are compared with the experimental results in Fig. 2. Although slight over-prediction in spreading is observed at instants t = 0.56 and 0.93 ms, good agreements in droplet retraction and rebound can be observed at later stages.

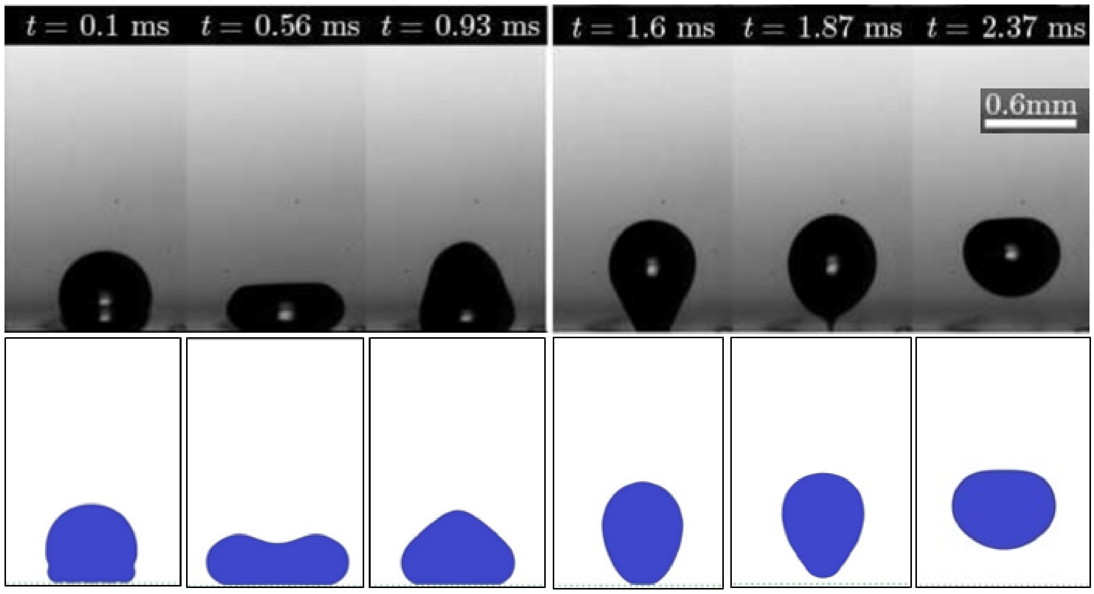

Fig. 2. Snapshots of droplet impacting on micro-textured surface. Top row: experimental results [44]**; Bottom row: current simulation results.**

In another validation case, the LBM results of droplet impact on a curved surface are compared with the Coupled Level Set and Volume of Fluid (CLSVOF) method [45]. The droplet and curved surface diameters are 1.76 mm and 4 mm, respectively. The impact velocity is 0.5 m/s. It seen from Fig. 3, the current LBM is able to capture droplet rebound from the curved surface with reasonable qualitative agreement.

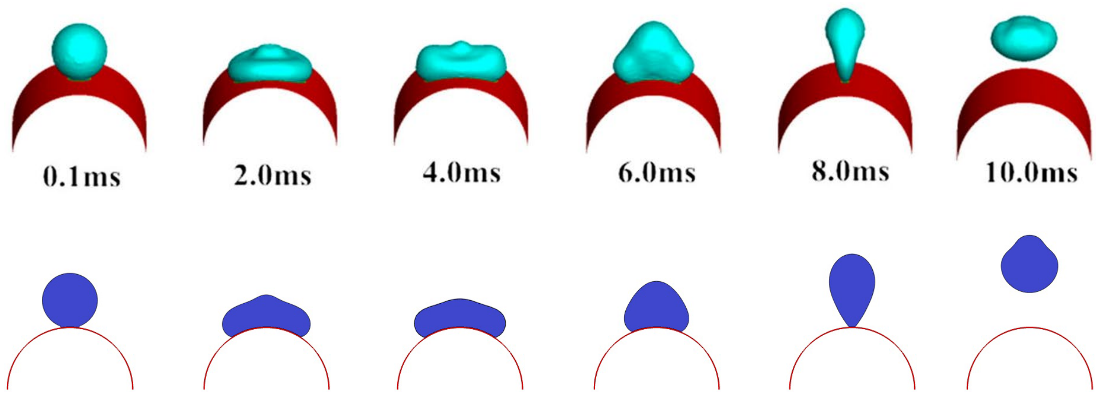

Fig. 3. Snapshots of droplet impacting on curved surface. Top row: CLSVOF results [45]**; Bottom row: current simulation results.**

4 Results and discussion

4.1 Baseline case

A case with the Weber number We = 19.6 and Reynolds number = 120, post height h/w = 7.5, inter-post spacing s/w = 2 and bump curvature w/R = 2/225 is analyzed as the baseline case. The evolution of the droplet's two spreading factors with several selected snapshots are shown in Fig. 4. It is seen that the droplet nearly jumps off the nano-structured bump after its first impact with only a small area remained in contact with the central post, and then impacts again (second impact) with much lower energy due to solid-liquid interactions and surface tension. As a result, the two spreading factors oscillate with time.

During the first half of the initial impact ($t^* < 1.53$), the impacting droplet penetrates to the inter-post gaps. The resulting lamella spreads both horizontally and vertically on the bump till achieving the maximum spreading $S^*_{x,max} = 1.74$ and $S^*_{y,max} = -0.082$ at $t^* = 1.53$ (Fig. 4(d)), which is also reflected by the velocity vectors in the droplet shown in Fig. 5(a). Note that the horizontal spreading evolves in a stepwise manner due to the separate posts (see the insets in Fig. 4).

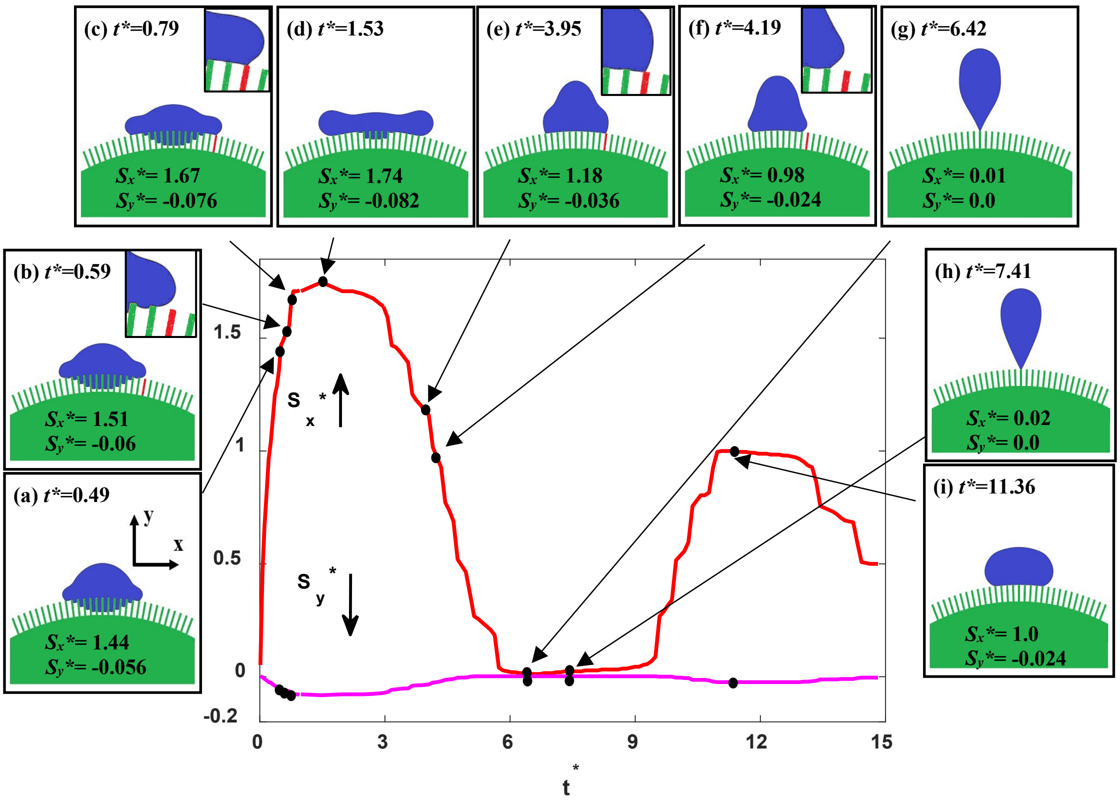

Fig. 4. Evolution of the spreading factors in the baseline case, where the post height h/w = 7.5, inter-post spacing s/w = 2.0, bump curvature w/R = 2/225, and the Weber number We = 19.6.

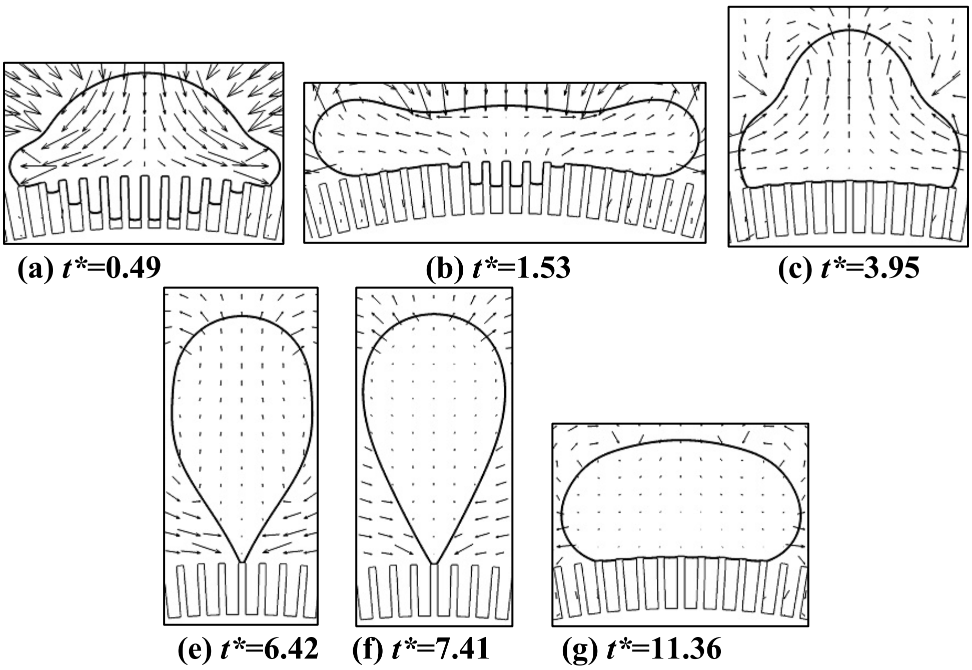

Fig. 5. Velocity vectors in the baseline case at selected instants.

From the energy point of view, the droplet's initial kinetic energy results in its penetration to the inter-post gaps. During this penetration process the kinetic energy is stored as the surface energy of the deformed droplet [46,47]. If the droplet's initial kinetic energy is high enough to collapse the air-pockets contained in inter-post gaps, the penetrating droop can touch the bottom surface, leading to the transition to the sticky Wenzel state.

During the second half of the initial impact ($1.53 < t^* < 7.41$), the surface tension plays a major role to retract the lamella (Figs. 4(e), 4(f) and 5(c)). Both the spreading factors reduce in magnitude, resulting in the decrease of surface area. The red color posts in subfigures (e and f) of Fig. 4 explain the formation of slightly vertical and horizontal variations of spreading factor S^*_x during the retraction process. The lamella quickly retracts back from red post at time t*=3.95 in subfigure(f) to neighboring green post at time t*=4.19, producing a slightly vertical segment of spreading factor (Fig. 4). Then, the retraction occurs on the post, producing a small roughly horizontal segment in spreading factor evolution curve. During droplet retraction process, the stored surface energy is transferred back into the kinetic energy. The lamella then gains an upward velocity due to the constraint from the underneath bump, nearly jumping off the bump (Figs. 4(g) and 4(h)).

After about $t^* = 7.41$, another spreading and retraction process occurs. However, due to the energy dissipation, the peak magnitudes of both horizontal and vertical spreading factors appearing at near $t^* = 11$ are much smaller than those in the first impact. This impacting process will repeat a few times till the droplet achieves its equilibrium state on the bump, which is not presented here since the present study mainly focuses on the droplet's dynamics in the first spreading and retraction cycle that is crucial to its final wetting state.

4.2 Effect of post height

Figure 6 compares the droplet impacting on bumps with three different post heights, i.e., $h/w = 0$ (bump with smooth surface), 2.5 and 7.5 (the baseline case). The corresponding evolutions of spreading factors are shown in Fig. 7. It is seen that both the maximum horizontal and maximum vertical spreading factors reduce with the post height, which is caused by increased room in the inter-post gaps and hence increased stored surface energy during the droplet penetration. For the bump with $h/w = 7.5$ (i.e., the baseline case), the liquid droop in the inter-post gaps never reaches the bottom surface, so that the droplet remains in the Cassie state. However, if the bump height reduces to $h/w = 2.5$, the liquid droop touches the bottom surface, leading to the Wenzel state.

From Fig. 7, it is also interesting to see that, although the spreading on different bumps during the first impact completes almost at the same instant, the ensuing droplet retraction on the textured bumps is generally faster than on the smooth bump. If the Cassie state occurs as in the $h/w = 7.5$ case, during the retraction more kinetic energy is transferred back from the stored surface energy, resulting in faster retraction. On the other hand, if the Wenzel state occurs as in the $h/w = 2.5$ case, the extent of retraction in the horizontal direction is significantly reduced due to the restriction from the wetted bump bottom surface. For this reason, the retraction process is completed even earlier.

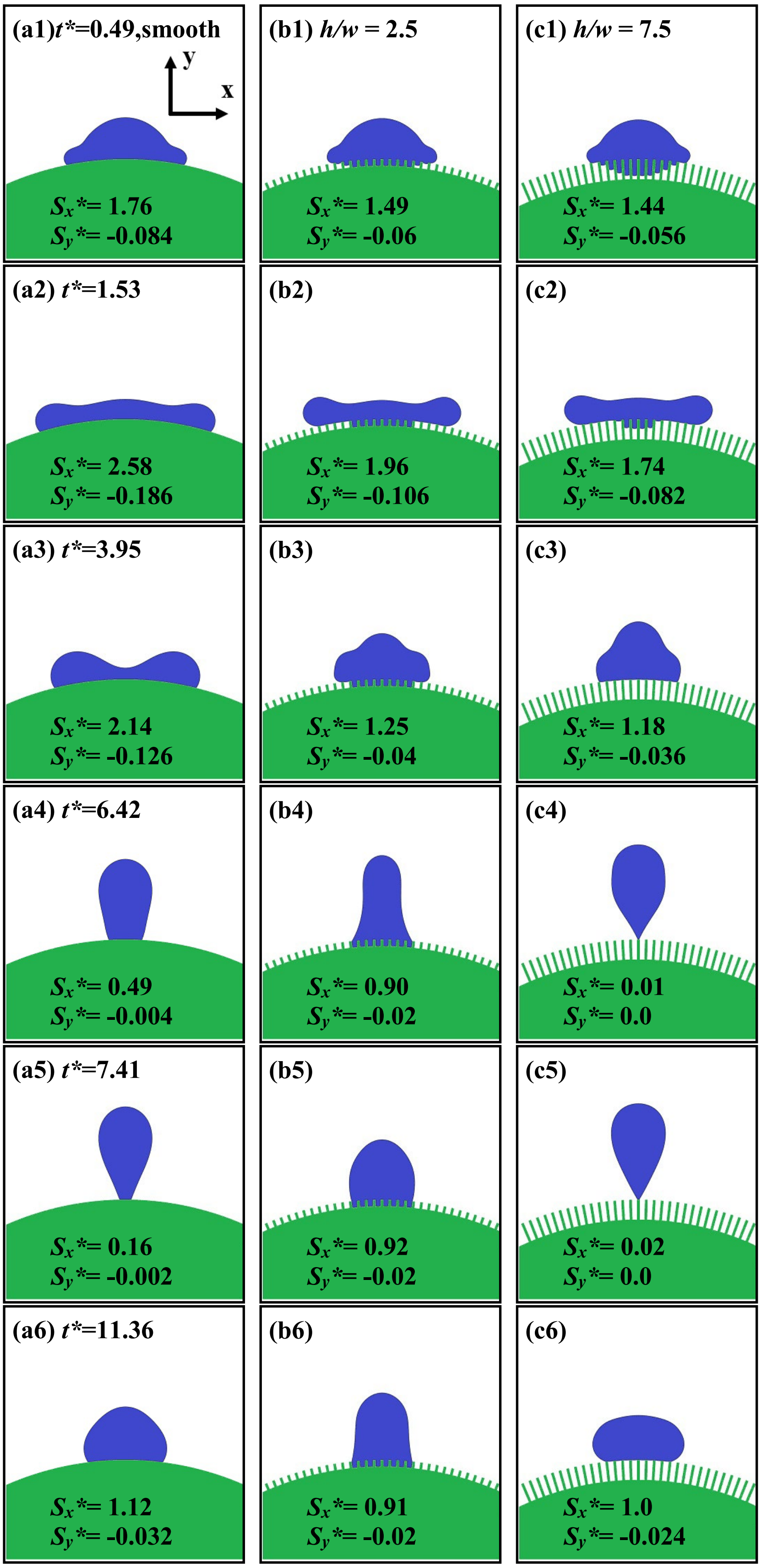

Fig. 6. Evolution of the droplet impact on bumps with different post heights.

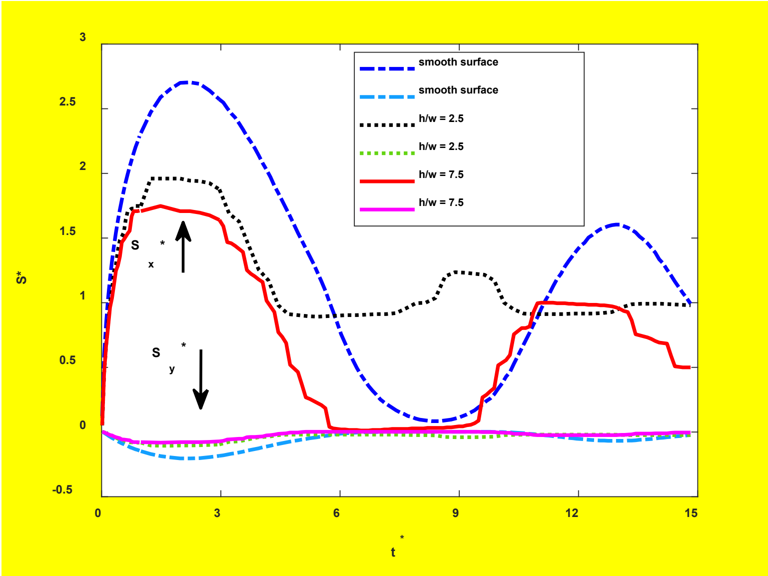

Fig. 7. Evolution of the spreading factors of droplet impact on bumps with different post heights.

4.3 Effect of inter-post spacing

Figure 8 shows the evolution of droplet impact on nano-textured bumps with different inter-post spacings, i.e., *s*/*w* = 1, 2 (the baseline case) and 3. It is seen that, since more liquid penetrates into inter-post gaps, the droplet horizontal and vertical spreading reduces with increasing the inter-post spacing, which is also confirmed by the spreading factor curves shown in Fig. 9. Droplet rebound is observed in the case with the smallest inter-post spacing *s*/*w* = 1 (see Fig. 8(a6)), the Cassie state is achieved in the baseline case with moderate inter-post spacing *s*/*w* = 2, and the Wenzel state is obtained in the case with the largest inter-post spacing *s*/*w* = 3 (see Fig. 8(c6)). The rebound appearing in the *s*/*w* = 1 case can be understood by generation of upward velocity due to vertical retraction [27]. As witnessed from Fig. 10 a larger upward velocity is produced due to the largest vertical retraction (see Fig. 9) combined with the surface-kinetic energy conversion of the initially penetrated liquid, leading to droplet rebound. On the contrary, the occurrence of the sticky Wenzel state significantly limits the spreading and retraction of the droplet.

If the inter-post spacing is further reduced, it is expected that the horizontal and vertical spreading will be further increased, as reflected by the snapshots and spreading factor curves in the extreme case, i.e., the smooth bump case discussed in Section 4.2. However, the reduced inter-post spacing also causes the increase of the contact area on the nano-textured bump, hence dissipates more energy through the friction between the liquid and the solid. In this case, the droplet may no longer has adequate surface-kinetic energy conversion to support rebound after the first impact [48], as reflected in the smooth bump case.

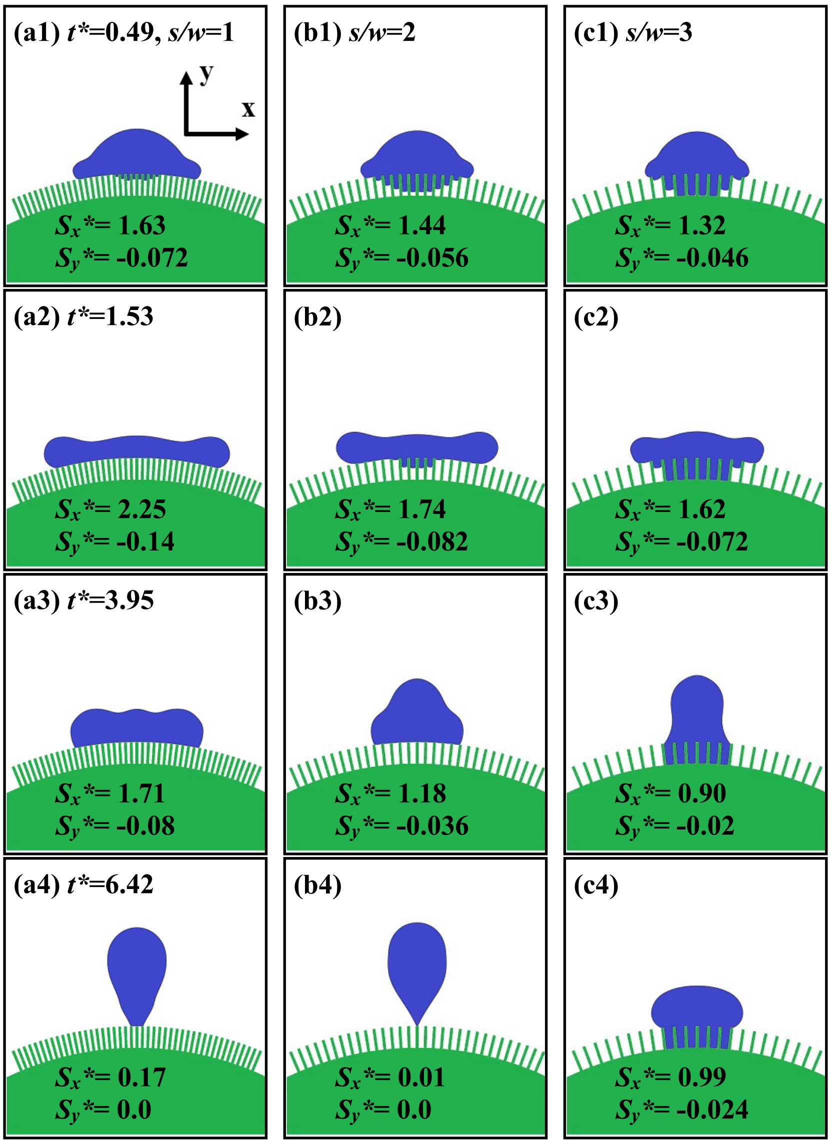

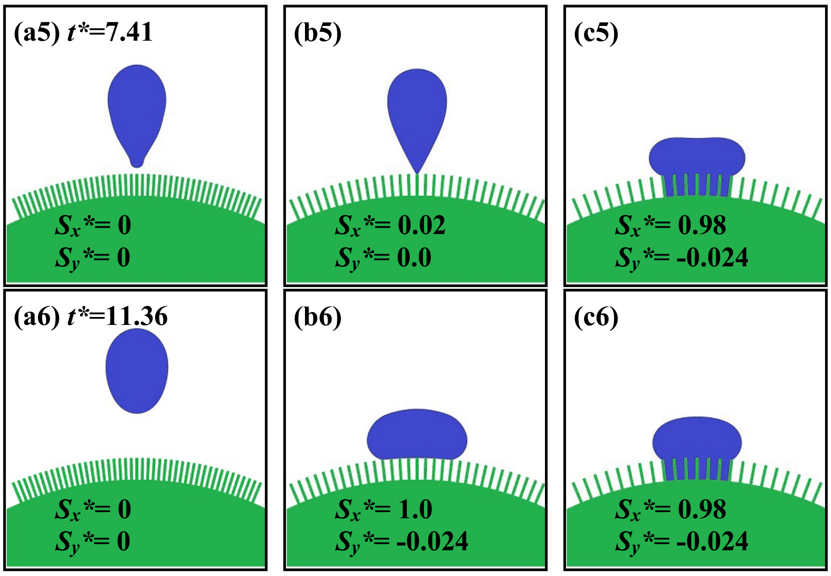

Fig. 8. Evolution of droplet impact on nano-textured bumps with different inter-post spacing: (a) *s/w* =1.0, (b) *s/w* =2.0, (c) *s/w* =3.0.

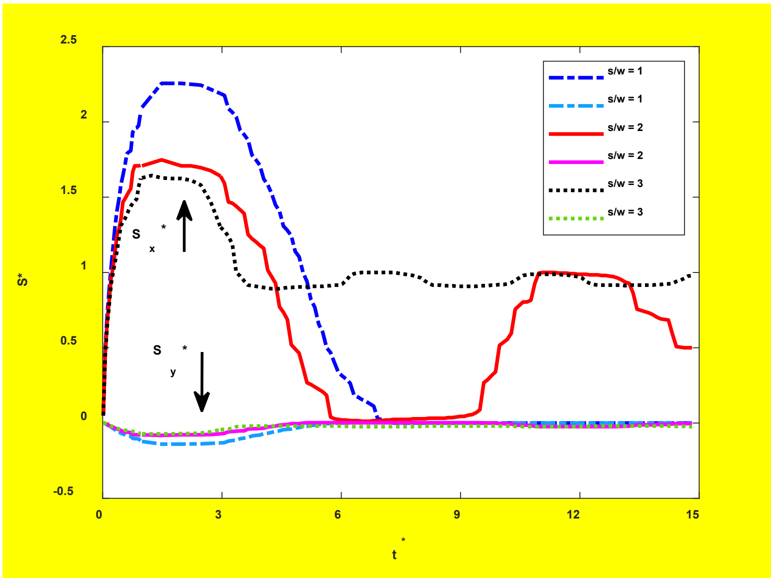

Fig. 9. Evolution of spreading factors of droplet impact on nano-textured bumps with different inter-post spacing: *s/w* =1.0, *s/w* =2.0, *s/w* =3.0.

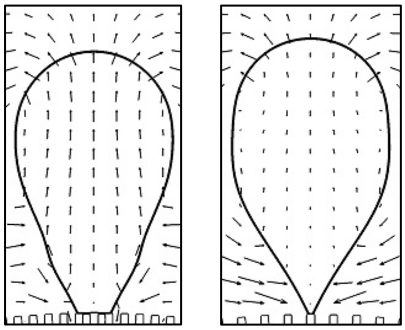

(a) (b)

Fig. 10. Velocity vectors during retraction phase at t^{*}= 6.42 for (a) inter-post spacing *s/w*=1.0, (b) inter-post spacing *s/w*=2.0.

4.4 Effect of bump curvature

Droplet dynamics on bumps with three different surface curvature, i.e., *w/R*= 2/75, 2/225 (the baseline case) and 2/900 are compared through selected snapshots in Fig. 11 and evolution of spreading factors in Fig. 12. It is seen from Fig. 11 that the droplet rebounds on the bump with the largest curvature, while assumes the Cassie state on the other two bumps.

When the bump is nearly flat with the smallest curvature *w/R* = 2/900, the horizontal spreading dominates over the negligible vertical spreading, as shown in Fig. 12. The maximum horizontal and vertical spreading factors are $S^{*}_{x,max}$ = 1.74 and $S^{*}_{y,max}$ = -0.0018, respectively, both appearing at t^{*} = 1.23. The increase of bump curvature allows the droplet to spread more in the vertical direction and even in the horizontal direction. As revealed in Fig. 12, the *w/R* = 2/225 bump has a similar maximum horizontal spreading but a much larger maximum vertical spreading $S^{*}_{y,max}$ = -0.082 as compared with the *w/R* = 2/900 bump. As for the *w/R* = 2/75 bump, both the maximum spreading factors increase significantly, i.e., $S^{*}_{x,max}$ = 1.83 and $S^{*}_{y,max}$ = -0.310.

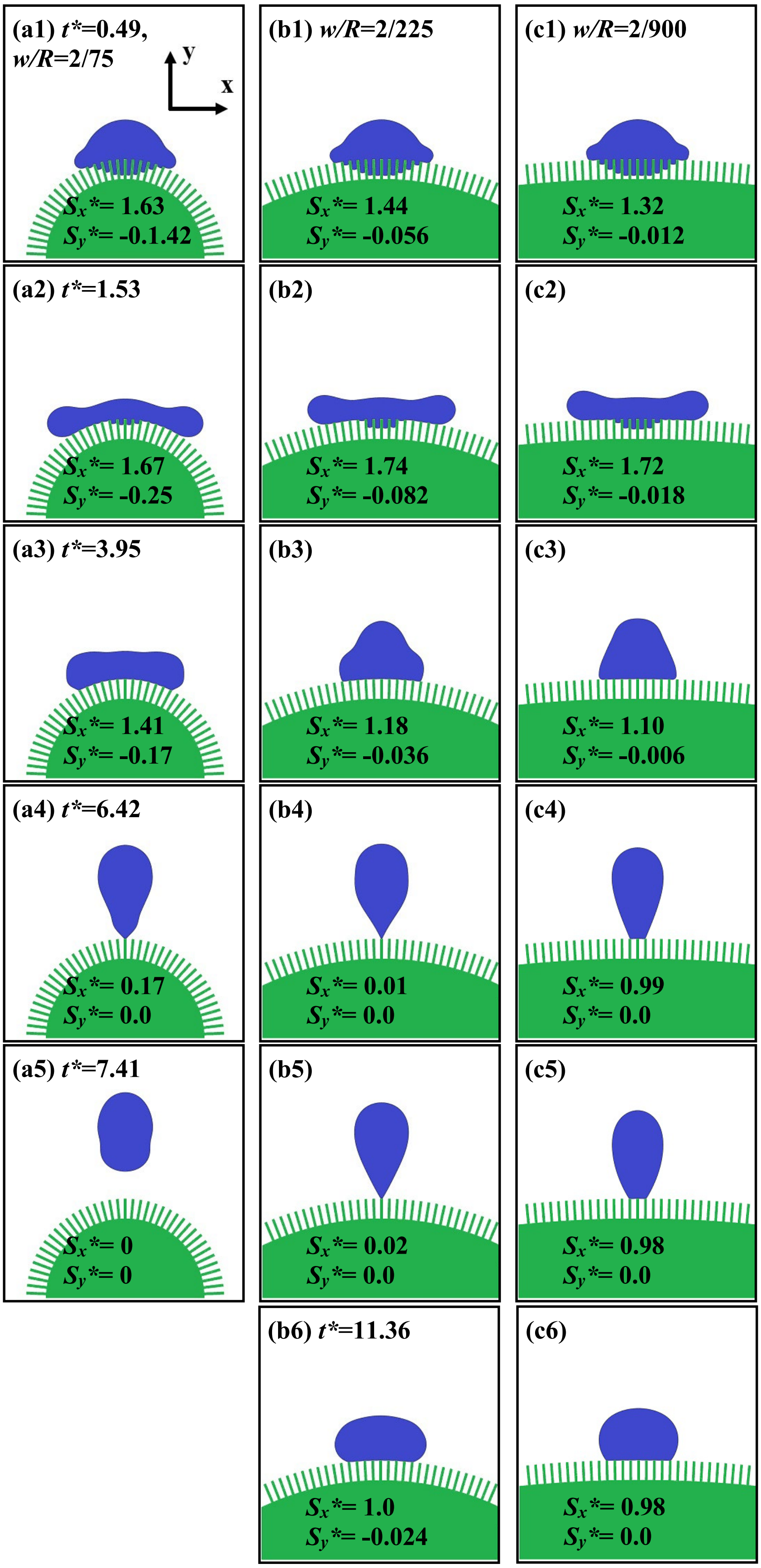
(a1) t*=0.49, w/R=2/75
y
x
Sx*= 1.63
Sy*= -0.1.42
(b1) w/R=2/225
Sx*= 1.44
Sy*= -0.056
(c1) w/R=2/900
Sx*= 1.32
Sy*= -0.012
(a2) t*=1.53
Sx*= 1.67
Sy*= -0.25
(b2)
Sx*= 1.74
Sy*= -0.082
(c2)
Sx*= 1.72
Sy*= -0.018
(a3) t*=3.95
Sx*= 1.41
Sy*= -0.17
(b3)
Sx*= 1.18
Sy*= -0.036
(c3)
Sx*= 1.10
Sy*= -0.006
(a4) t*=6.42
Sx*= 0.17
Sy*= 0.0
(b4)
Sx*= 0.01
Sy*= 0.0
(c4)
Sx*= 0.99
Sy*= 0.0
(a5) t*=7.41
Sx*= 0
Sy*= 0
(b5)
Sx*= 0.02
Sy*= 0.0
(c5)
Sx*= 0.98
Sy*= 0.0
(b6) t*=11.36
Sx*= 1.0
Sy*= -0.024
(c6)
Sx*= 0.98
Sy*= 0.0

Fig. 11. Evolution of droplet impact on nano-textured bumps with different bump curvature: (a) w/R =2/75, (b) w/R =2/225, (c) w/R =2/900.

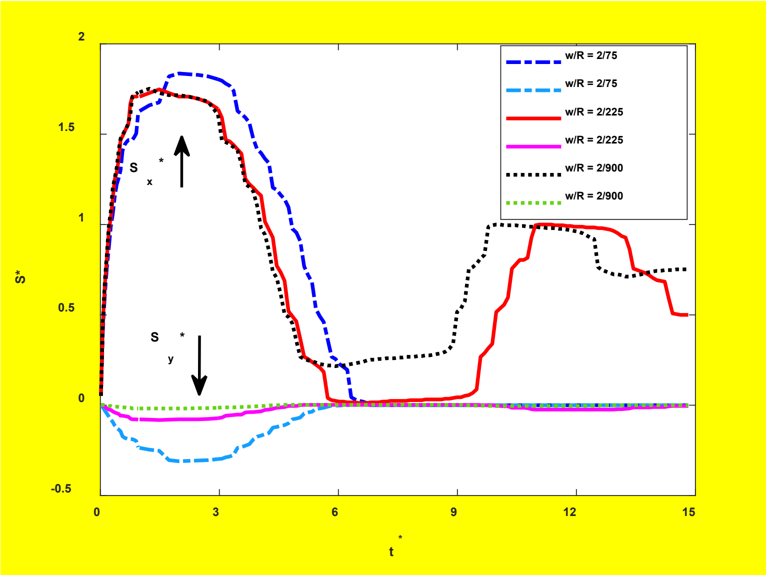

Fig. 12. Evolution of spreading factors for nano-textured bumps with different bump curvature: w/R =2/75, w/R =2/225, w/R =2/900.

4.5 Effect of impact speed

Figure 13 compares the dynamics of droplet impacting on a bump with three different impact speeds, i.e., 9 m/s, 12 m/s and 15 m/s, corresponding to the Weber number We = 11.0, 19.6 (the baseline case) and 30.6, respectively. Apparently increasing the Weber number increases the penetrating droop depth. With the highest impact speed as in the We = 30.6 case, the liquid droop touches the bottom surface very soon leading to the Wenzel transition (Fig. 13(c1)). In the other two cases with lower Weber numbers, the Cassie state is achieved (Figs. 13(a6) and 13(b6)).

The spreading factor evolution curves shown in Fig. 14 reveal that the maximum horizontal and vertical spreading factors both increase with the Weber number simply due to the increase of kinetic energy carried by the impacting droplet. The time required to achieve the maximum spreading factors are t^* = 0.91, 1.53 and 1.7, respectively, also increasing with the Weber number.

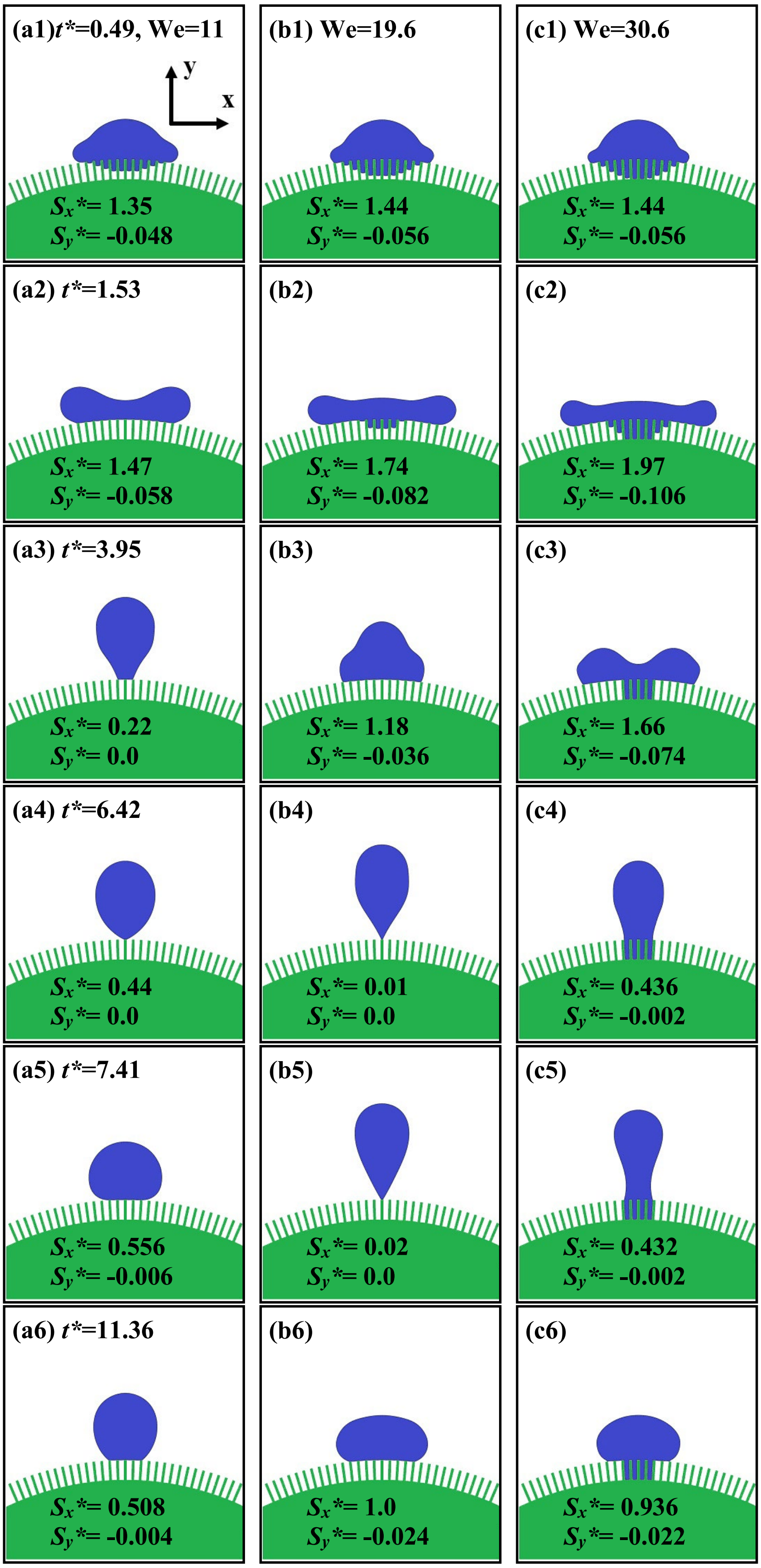

Fig. 13. Evolution of droplet impact on nano-textured bumps with different Weber numbers (a) We=11 (b) We=19.6 and (c) We=30.6.

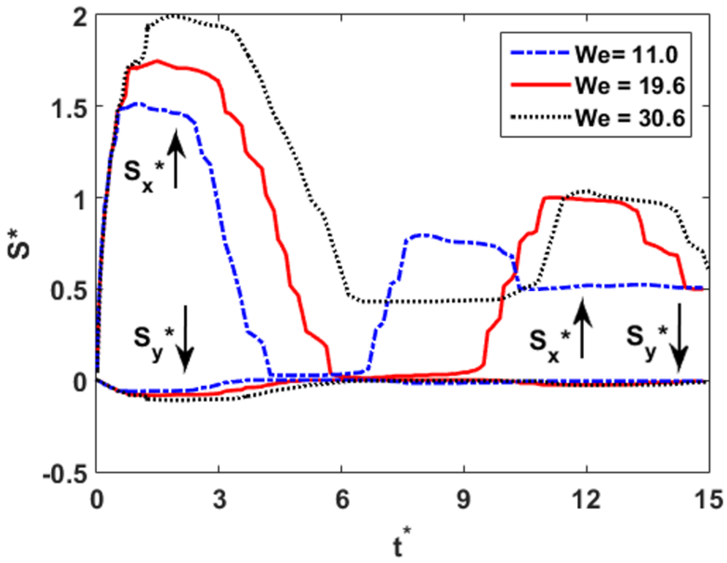

Fig. 14. Evolution of spreading factors of droplet impact on nano-textured bumps with different Weber numbers.

4.6 Parametric maps describing the state of impacting droplet

A comprehensive view of the dependence of the impacting droplet's wetting state on the bump parameters is presented in Fig. 15, where the Weber number is represented by square markers. In Fig. 15(a), the inter-post spacing varies from s/w = 1 to 5 and the post height varies from h/w = 1.25 to 12.5, while the bump curvature is fixed at w/R = 2/225. If the droplet's impact speed increases from 0 to 15 m/s (equivalently the Weber number increases from 0 to 30.6), three types of interfaces are captured: the blue interface (region 1) separates the Cassie state for Weber number less than the shown values from the Wenzel state for Weber number not less than the shown values, the orange interface (region 2) separates the Cassie state for Weber number less than the shown values from the rebound state for Weber number not less than the shown values, and the green interface (region 3) separates the Cassie state for Weber number less than the shown values from the rebound state for Weber number equal to the shown values and the Wenzel state for Weber number greater than the shown values. From these interfaces, one can see that, on bumps with tall posts and narrow inter-post spacing, the Cassie state is dominant at small to moderate Weber numbers, whereas the droplet rebounds at high Weber numbers. On the other hand, on bumps with short posts and wide inter-post spacing, the Wenzel state can be obtained easily even at very small Weber numbers. Furthermore, the green interface indicates that on bumps with tall posts and moderate inter-post spacing, the state of the droplet depends very much on the droplet's impact speed: with the increase of speed, the droplet can experience different wetting dynamics from the Cassie state, rebound to the Wenzel state.

Fig. 15(b) further includes the bump curvature, which varies from $w/R = 2/75$ to $2/900$, while fixing the inter-post spacing at $s/w = 2$. In addition to the three types of interfaces (regions 1-3) presented in Fig. 15(a), Fig. 15(b) also presents a gray interface (region 4), which indicates that the Cassie state holds throughout the entire range of investigated Weber numbers. From all these interfaces, one can see that, on bumps with short posts, the Wenzel state is dominant no matter how curved the bump surface is. On bumps with high posts, however, the bump curvature matters: when the bump is less curved, the droplet remains the Cassie state throughout the entire range of the investigated Weber numbers, whereas when the bump is more curved, the droplet tends to rebound if the impact speed is large enough.

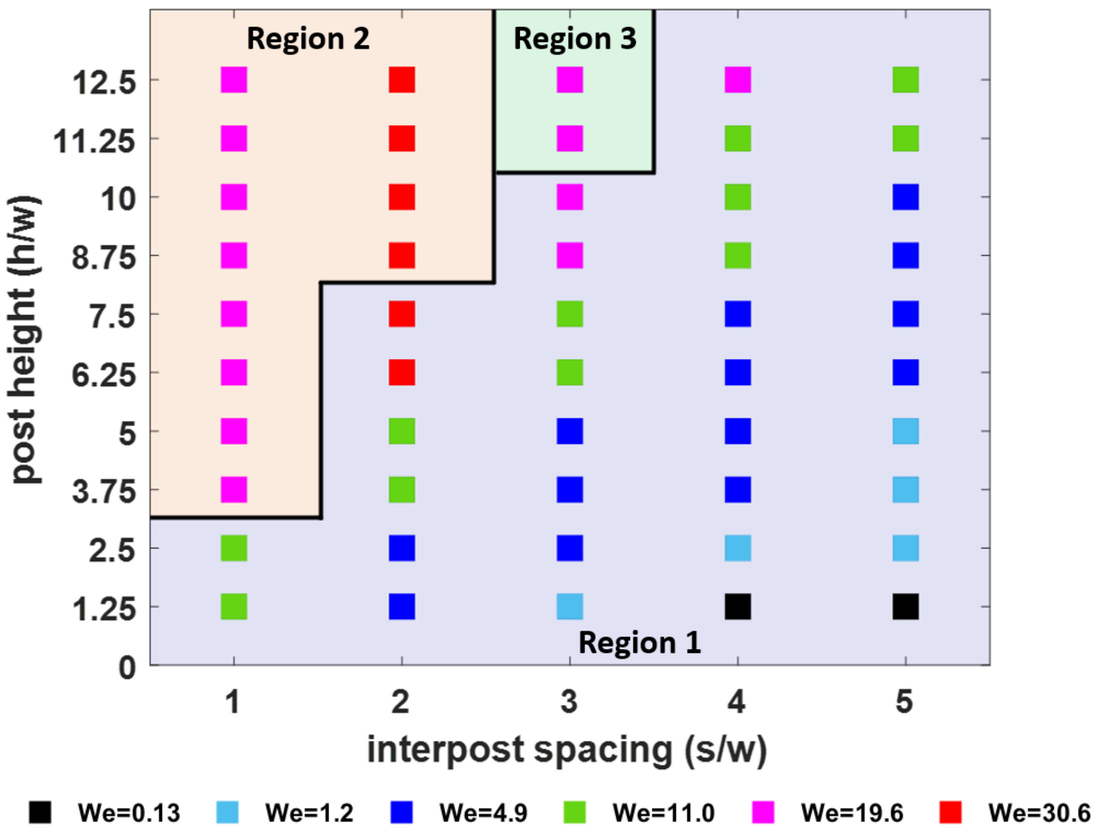

(a)

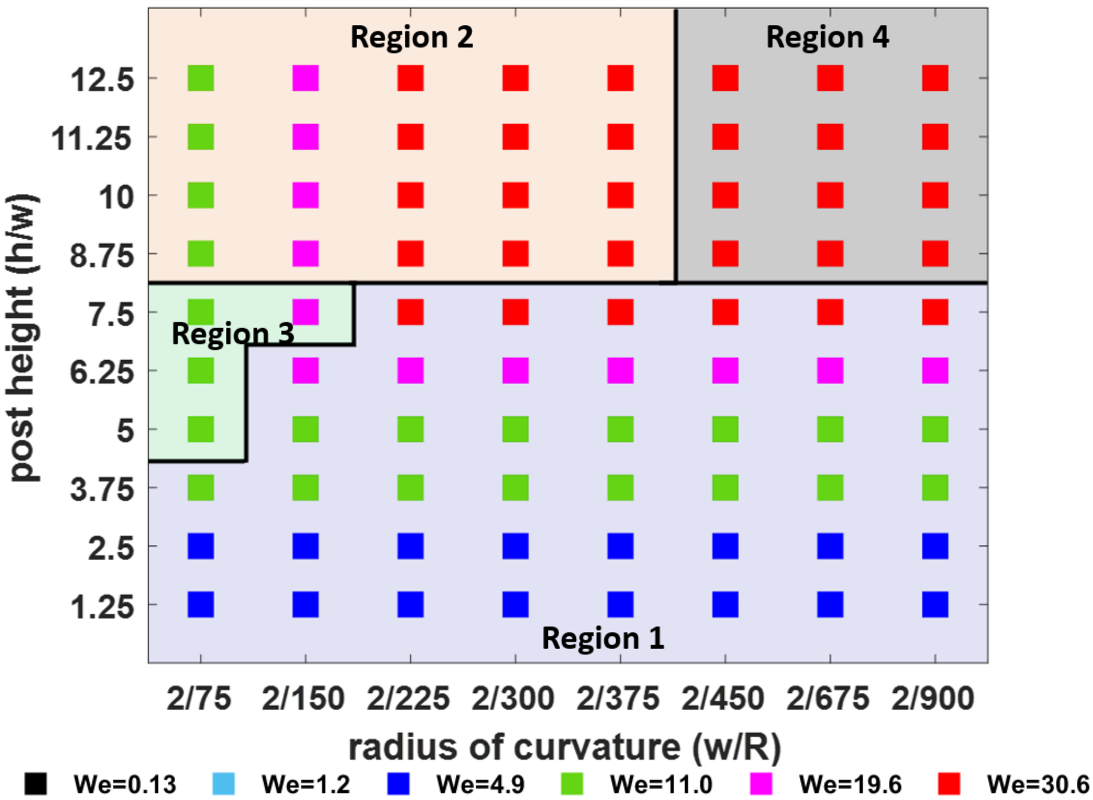

(b)

Fig. 15. (a) Parametric map spanned by the post height, interpost spacing and Weber number, where the bump curvature is fixed at *w/R* = 2/225 (b) Parametric map spanned by the post height, bump surface curvature and Weber number, where the inter-post spacing is fixed at *s/w* = 2. Region 1 (in blue): interface between the Cassie state (when the Weber number is less than values shown by square makers in the region) and the Wenzel state (when the Weber number is equal to or greater than values shown by square makers in the region); region 2 (in orange): interface between the Cassie state (when the Weber number is less than values in the region) and the rebound (when the Weber number is equal to or greater than values in the region); region 3 (in green): interface between the Cassie state (when the Weber number is less than values in the region) and the rebound (when the Weber number is equal to values in the region) and the Wenzel state (when the Weber number is greater than values in the region); region 4 (in grey): no change of the Cassie state in the investigated We range. The square markers represent the different values of Weber number by different colors.

It is particularly meaningful to examine the droplet dynamics at a moderate and possibly mean impact speed, say $U = 6$ m/s (corresponding to We = 4.9). Since droplets in the Cassie state remain suspended on the nanostructures and are much easier to collect compared to those in the Wenzel or rebound state, the Cassie state is desirable for fog water harvesting. Fig. 16(a) depicts a roughly straight boundary between the Cassie state and the Wenzel state. At the moderate impact speed, the Cassie state can be achieved for nearly all posts if the interpost spacing is small but only for larger posts if the interpost spacing is wide, when the bump curvature is mild, e.g., at $w/R = 2/225$. Fig. 16(b) further reveals that, when the inter-post spacing is fixed at $s/w = 2$, the droplet is in the Cassie state if the bump curvature is smaller than $w/R = 2/150$. The bump curvature seems to have very little influence on the droplet state.

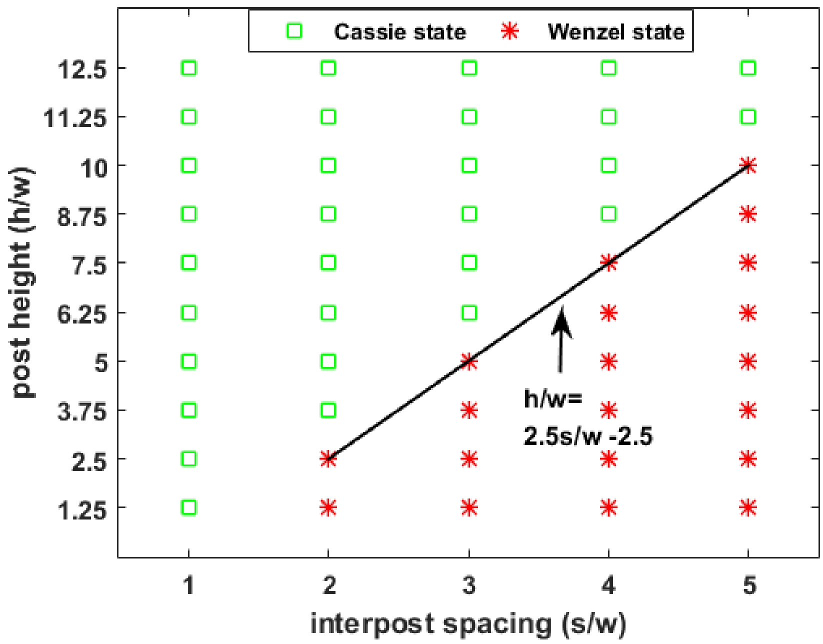

(a)

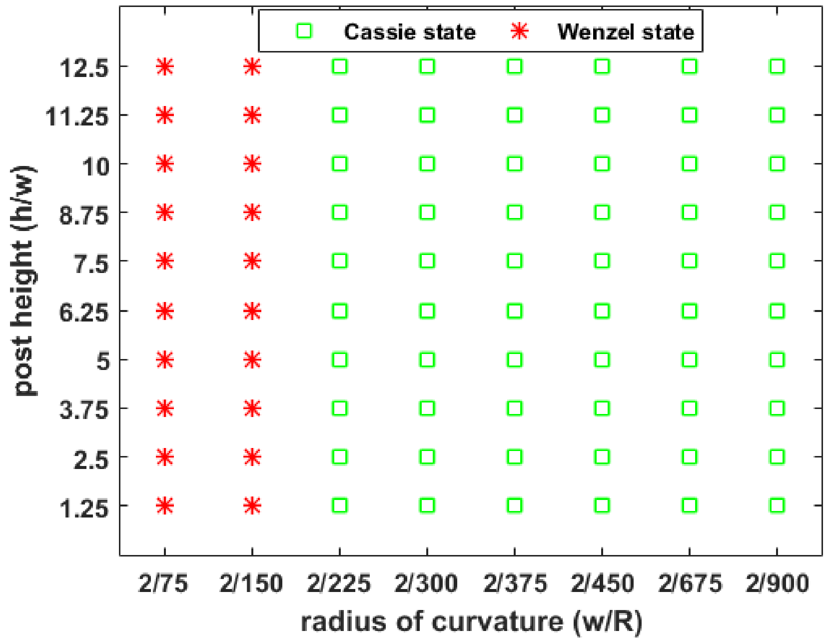

(b)

Fig. 16. Parametric maps showing the state of droplet dynamics when the droplet impact speed is moderate (*U* = 6 m/s, We = 4.9): (a) map spanned by the post height and inter-post spacing, where the bump curvature is fixed at *w/R* = 2/225 (b) map spanned by the post height and bump surface curvature, where the inter-post spacing is fixed at *s/w* = 2.

5 Conclusions

In this work, LBM-based simulations were conducted to study the dynamics of single fog droplet impacting on desert beetle inspired nano-textured bumps. The focus was placed on several key parameters, including post height, inter-post spacing, bump curvature and impact speed. Parametric maps describing the state of impacting droplet (i.e., the Cassie state, the Wenzel state or rebound) were obtained. The major conclusions are summarized as follows:

1. Adding nano-posts on a bump surface changes the morphology of droplet during the impact. That is, the penetration of droplet to the inter-post gaps causes the reduction of droplet spreading. If the penetration is so deep that the droplet touches the bottom surface, the undesirable Wenzel state occurs.

2. The separate posts reduce the total area on the bump top surface, which greatly reduces frictional dissipation during the impact. As a result, the droplet can retract with higher energy if appropriate inter-post spacing is adopted.
3. The droplet impact speed needs to be low or moderate (approximately $U < 6$ m/s or We < 4.9 in this study) to ensure the occurrence of the desirable Cassie state. On the contrary, too large impact speeds can result in either the Wenzel state or rebound.
4. At moderate impact speeds, the post needs to be sufficiently high and the inter-post spacing needs to be sufficiently small to achieve the desirable Cassie state. If these conditions are satisfied, the bump curvature only plays a marginal role.

Note this study is still very limited since some parameters were fixed. However, it has shed some lights on the physics and design of desert beetle inspired bumps for fog water harvesting. In the near future, we will continue this study in a larger parameter space and with more realistic parameter values.

Acknowledgement

The authors gratefully acknowledge the financial support for this study from The Research Grants Council of Hong Kong under General Research Fund (Project No. 15214418).

References

[1] M. Kummu, P.J. Ward, H. De Moel, O. Varis, Is physical water scarcity a new phenomenon? Global assessment of water shortage over the last two millennia, Environ. Res. Lett. 5 (2010). https://doi.org/10.1088/1748-9326/5/3/034006.

[2] J.R. Henschel, M.K. Seely, Ecophysiology of atmospheric moisture in the Namib Desert, Atmos. Res. 87 (2008) 362–368. https://doi.org/10.1016/j.atmosres.2007.11.015.

[3] A.R. Parker, C.R. Lawrence, Water capture by a desert beetle, Nature. 414 (2001) 33–34. https://doi.org/10.1038/35102108.

[4] S. Choo, H.J. Choi, H. Lee, Water-collecting behavior of nanostructured surfaces with special wettability, Appl. Surf. Sci. 324 (2015) 563–568. https://doi.org/10.1016/j.apsusc.2014.10.061.

[5] J. Guadarrama-Cetina, A. Mongruel, M.G. Medici, E. Baquero, A.R. Parker, I. Milimouk-Melnytchuk, W. González-Viñas, D. Beysens, Dew condensation on desert beetle skin, Eur. Phys. J. E. 37 (2014). https://doi.org/10.1140/epje/i2014-14109-y.

[6] B. White, A. Sarkar, A.M. Kietzig, Fog-harvesting inspired by the Stenocara beetle - An analysis of drop collection and removal from biomimetic samples with wetting contrast, Appl. Surf. Sci. 284 (2013) 826–836. https://doi.org/10.1016/j.apsusc.2013.08.017.

[7] Y. Hou, M. Yu, X. Chen, Z. Wang, S. Yao, Recurrent filmwise and dropwise condensation on a beetle mimetic, 9 (2014) 71–81.

[8] J.K. Domen, W.T. Stringfellow, M. Kay, C. Shelly, Fog water as an alternative and sustainable water resource, Clean Techn Env. Policy. 16 (2014) 235–249. https://doi.org/10.1007/s10098-013-0645-z.

[9] A.L. Yarin, Drop Impact Dynamics: Splashing, Spreading, Receding, Bouncing…, Annu. Rev. Fluid Mech. 38 (2006) 159–192. https://doi.org/10.1146/annurev.fluid.38.050304.092144.

[10] Š. Šikalo, C. Tropea, E.N. Ganić, Impact of droplets onto inclined surfaces, J. Colloid Interface Sci. 286 (2005) 661–669. https://doi.org/10.1016/j.jcis.2005.01.050.

[11] S.F. Lunkad, V. V. Buwa, K.D.P. Nigam, Numerical simulations of drop impact and spreading on horizontal and inclined surfaces, Chem. Eng. Sci. 62 (2007) 7214–7224. https://doi.org/10.1016/j.ces.2007.07.036.

[12] C. Shen, C. Yu, Y. Chen, Spreading dynamics of droplet on an inclined surface, Theor. Comput. Fluid Dyn. 30 (2016) 237–252. https://doi.org/10.1007/s00162-015-0377-2.

[13] S. Ahmad, H. Tang, H. Yao, Oblique impact of two successive droplets on a flat surface, Int. J. Heat Mass Transf. 119 (2018) 433–445. https://doi.org/10.1016/J.IJHEATMASSTRANSFER.2017.11.129.

[14] W.Z. Yuan, L.Z. Zhang, Lattice Boltzmann simulation of droplets impacting on superhydrophobic surfaces with randomly distributed rough structures, Langmuir. 33 (2017) 820–829. https://doi.org/10.1021/acs.langmuir.6b04041.

[15] S. Chen, V. Bertola, Drop impact on spherical soft surfaces, Phys. Fluids. 29

(2017). https://doi.org/10.1063/1.4996587.

[16] Y. Liu, M. Andrew, J. Li, J.M. Yeomans, Z. Wang, Symmetry-breaking in drop bouncing on curved surfaces, Nat. Commun. 6 (2015) 1–8. https://doi.org/10.1038/ncomms10034.

[17] D. Khojasteh, A. Bordbar, R. Kamali, M. Marengo, Curvature effect on droplet impacting onto hydrophobic and superhydrophobic spheres, Int. J. Comut. Fluid Dyn. 31 (2017) 310–323. https://doi.org/10.1080/10618562.2017.1349312.

[18] Y.C. Jung, B. Bhushan, Dynamic effects of bouncing water droplets on superhydrophobic surfaces, Langmuir. 24 (2008) 6262–6269. https://doi.org/10.1021/la8003504.

[19] P. Hao, C. Lv, F. Niu, Y. Yu, Water droplet impact on superhydrophobic surfaces with microstructures and hierarchical roughness, Sci. China Physics, Mech. Astron. 57 (2014) 1376–1381. https://doi.org/10.1007/s11433-014-5472-7.

[20] D.J. Lee, H.M. Kim, Y.S. Song, J.R. Youn, Water droplet bouncing and superhydrophobicity induced by multiscale hierarchical nanostructures, ACS Nano. 6 (2012) 7656–7664. https://doi.org/10.1021/nn3032547.

[21] M. McCarthy, K. Gerasopoulos, R. Enright, J.N. Culver, R. Ghodssi, E.N. Wang, Biotemplated hierarchical surfaces and the role of dual length scales on the repellency of impacting droplets, Appl. Phys. Lett. 100 (2012). https://doi.org/10.1063/1.4729935.

[22] H. Kim, C. Lee, M.H. Kim, J. Kim, Drop impact characteristics and structure effects of hydrophobic surfaces with micro- and/or nanoscaled structures, Langmuir. 28 (2012) 11250–11257. https://doi.org/10.1021/la302215n.

[23] Z. Wang, C. Lopez, A. Hirsa, N. Koratkar, Impact dynamics and rebound of water droplets on superhydrophobic carbon nanotube arrays, Appl. Phys. Lett. 91 (2007). https://doi.org/10.1063/1.2756296.

[24] A.I. Aria, M. Gharib, Physicochemical characteristics and droplet impact dynamics of superhydrophobic carbon nanotube arrays, Langmuir. 30 (2014) 6780–6790. https://doi.org/10.1021/la501360t.

[25] G. Kwak, D.W. Lee, I.S. Kang, K. Yong, G. Kwak, D.W. Lee, I.S. Kang, K. Yong, A study on the dynamic behaviors of water droplets impacting

nanostructured surfaces, 042139 (2012). https://doi.org/10.1063/1.3662046.
[26] P. Tsai, S. Pacheco, C. Pirat, L. Lefferts, D. Lohse, Drop impact upon micro- and nanostructured superhydrophobic surfaces, 25 (2009) 12293–12298. https://doi.org/10.1021/la900330q.
[27] Y. Shen, S. Liu, C. Zhu, J. Tao, Z. Chen, H. Tao, L. Pan, G. Wang, T. Wang, Bouncing dynamics of impact droplets on the convex superhydrophobic surfaces, 221601 (2017). https://doi.org/10.1063/1.4984230.
[28] R.S. Schemenauer, P.I. Joe, The collection efficiency of a massive fog collector, Atmos. Res. 24 (1989) 53–69. https://doi.org/10.1016/0169-8095(89)90036-7.
[29] X. Chen, J. Wu, R. Ma, M. Hua, N. Koratkar, S. Yao, Z. Wang, Nanograssed Micropyramidal Architectures for Continuous Dropwise Condensation, (2011) 4617–4623. https://doi.org/10.1002/adfm.201101302.
[30] X. Chen, R. Ma, H. Zhou, X. Zhou, L. Che, S. Yao, Z. Wang, Activating the microscale edge effect in a hierarchical surface for frosting suppression and defrosting promotion, (2013) 1–8. https://doi.org/10.1038/srep02515.
[31] N. Miljkovic, R. Enright, E.N. Wang, Growth dynamics during dropwise condensation on nanostructured superhydrophobic surfaces, in: MNHMT2012, Atlanta, Georgia, USA, 2012.
[32] D.M. Fernandez, A. Torregrosa, P.S. Weiss-Penzias, B.J. Zhang, D. Sorensen, R.E. Cohen, G.H. McKinley, J. Kleingartner, A. Oliphant, M. Bowman, Fog water collection effectiveness: mesh intercomparisons, Aerosol Air Qual. Res. 18 (2018) 270–283. https://doi.org/10.4209/aaqr.2017.01.0040.
[33] H. Huang, M.C. Sukop, X.-Y. Lu, Introduction, in: Multiph. Lattice Boltzmann Methods Theory Appl., John Wiley & Sons, Ltd, 2015: pp. 1–17. https://doi.org/10.1002/9781118971451.ch1.
[34] Q. Li, K.H. Luo, X.J. Li, Lattice Boltzmann modeling of multiphase flows at large density ratio with an improved pseudopotential model, Phys. Rev. E - Stat. Nonlinear, Soft Matter Phys. 87 (2013). https://doi.org/10.1103/PhysRevE.87.053301.
[35] S. Chen, G.D. Doolen, Lattice Boltzmann Method for fluid flows, 30 (1998) 329–364. https://doi.org/10.1007/978-3-540-27982-2.
[36] D. Raabe, Overview of the lattice Boltzmann method for nano- and microscale

fluid dynamics in materials science and engineering, Model. Simul. Mater. Sci. Eng. 12 (2004) R13–R46. https://doi.org/10.1088/0965-0393/12/6/R01.

[37] A. A. Mohammed, Lattice Boltzmann method: fundamentals and engineering applications with computer codes, 2012. https://doi.org/10.2514/1.J051744.

[38] R. Benzi, S. Succi, M. Vergassola, The lattice Boltzmann equation: theory and applications, Phys. Rep. 222 (1992) 145–197. https://doi.org/10.1016/0370-1573(92)90090-M.

[39] X. Shan, H. Chen, Simulation of nonideal gases and liquid-gas phase transitions by the lattice Boltzmann equation, Phys. Rev. E. 49 (1994) 2941–2948. https://doi.org/10.1103/PhysRevE.49.2941.

[40] R. Benzi, L. Biferale, M. Sbragaglia, S. Succi, F. Toschi, Mesoscopic modeling of a two-phase flow in the presence of boundaries: The contact angle, Phys. Rev. E - Stat. Nonlinear, Soft Matter Phys. 74 (2006) 1–14. https://doi.org/10.1103/PhysRevE.74.021509.

[41] Z. Guo, C. Zheng, Analysis of lattice Boltzmann equation for microscale gas flows: Relaxation times, boundary conditions and the Knudsen layer, in: Int. J. Comut. Fluid Dyn., 2008. https://doi.org/10.1080/10618560802253100.

[42] P. Lallemand, L.-S. Luo, Theory of the lattice Boltzmann method: Dispersion, dissipation, isotropy, Galilean invariance, and stability, Phys. Rev. E. 61 (2000) 6546–6562. https://doi.org/10.1103/PhysRevE.61.6546.

[43] X. Shan, H. Chen, Lattice Boltzmann model for simulating flows with multi phases and components, Phys. Rev. E. 47 (1993) 1815–1819. https://doi.org/10.1103/PhysRevE.47.1815.

[44] T. Bobinski, G. Sobieraj, M. Psarski, G. Celichowski, J. Rokicki, Droplet bouncing on the surface with micro-structure, Arch. Mech. 69 (2017) 177–193.

[45] X. Liu, Y. Zhao, S. Chen, S. Shen, X. Zhao, Numerical research on the dynamic characteristics of a droplet impacting a hydrophobic tube, Phys. Fluids. 29 (2017) 62105. https://doi.org/10.1063/1.4986526.

[46] Y. Liu, L. Moevius, X. Xu, T. Qian, J.M. Yeomans, Z. Wang, Pancake bouncing on superhydrophobic surfaces, Nat. Phys. 10 (2014) 515–519. https://doi.org/10.1038/nphys2980.

[47] X. Deng, F. Schellenberger, P. Papadopoulos, D. Vollmer, H.J. Butt, Liquid

drops impacting superamphiphobic coatings, Langmuir. 29 (2013) 7847–7856. https://doi.org/10.1021/la401120j.

[48] L. Moevius, Y. Liu, Z. Wang, J.M. Yeomans, Pancake bouncing: Simulations and theory and experimental verification, Langmuir. 30 (2014) 13021–13032. https://doi.org/10.1021/la5033916.